Computer Modeling in Engineering & Sciences

Tech Science Press

https://doi.org/10.32604/cmes.2026.083905

ARTICLE

Entropy Generation Analysis of Alumina-Water Nanofluid Turbulent Convective Heat Transfer Using an Elliptic Blending Turbulence Model

Lei Yang[1,2], **Yiyun Hu**[1] **and Xianglong Yang**[1,*]

[1]College of Civil and Transportation Engineering, Shenzhen University, Shenzhen, China
[2]Key Laboratory for Resilient Infrastructures of Coastal Cities (MOE), Shenzhen University, Shenzhen, China

*Corresponding Author: Xianglong Yang. Email: xlyang@szu.edu.cn

Received: 13 April 2026; Accepted: 05 June 2026; Published: 27 July 2026

ABSTRACT: Accurate prediction of entropy generation in nanofluid turbulent convection is essential for optimizing thermal system efficiency, yet remains challenging due to complex near-wall phenomena and thermal property variations with temperature. This study applied an elliptic blending turbulence model (SST k-ω-φ-α) to numerically analyze entropy generation in alumina-water nanofluid flow through a uniformly heated circular tube. The model's performance was validated using both experimental data and established heat transfer and fluid flow correlations at small wall-bulk temperature difference condition, and its superiority was rigorously evaluated against two widely adopted turbulence models (SST k-ω and realizable k-ε). Results show that the SST k-ω-φ-α model demonstrates superior accuracy, with maximum deviations from classical Bejan's correlations of only 3.75% in heat transfer irreversibility and 1.86% in friction irreversibility, both of which are lower than the deviations of the comparative turbulence models. The SST k-ω-φ-α model was further used to analyze the entropy generation under large wall-bulk temperature difference condition. It was found that the failure of classical Bejan's correlation is due to the dominant influence of wall temperature on property evaluations and entropy mechanisms. Under large wall-bulk temperature difference condition, total entropy generation varies non-monotonically with Reynolds number (Re), revealing an optimal flow rate that minimizes irreversibility. On the whole, the effect of nanoparticle concentration depends on flow regime, being beneficial at low Re but detrimental at high Re. This work underscores the necessity of employing advanced numerical tools which are capable of resolving detailed near-wall physics using high-fidelity turbulence modeling, especially under significant temperature gradients, for reliable performance prediction in advanced thermal systems using nanofluids.

KEYWORDS: Entropy generation analysis; nanofluids; numerical simulation; elliptic blending turbulence model

1 Introduction

Nanofluids are a class of tailored colloidal suspensions comprising solid nanoparticles (typically 1–100 nm in diameter) evenly dispersed in conventional base fluids. Since the concept was first introduced by Choi and Eastman in 1995 [1], nanofluids have garnered widespread research interest owing to their adjustable thermal properties, such as superior thermal conductivity and remarkable stability. These attributes make them highly promising for use in high-performance heat exchangers and advanced energy systems.

Recent decades have witnessed a remarkable expansion in nanofluids research. Substantial efforts have concentrated on heat transfer enhancement using nanofluids in circular tubes. For conciseness, only selected representative studies are focused here. Some researchers have conducted systematic experimental studies on heat transfer of nanofluids [2–6]. The common conclusions drawn from these studies are: on the one

hand, regardless of the materials used for nanoparticles and base fluid, the heat transfer coefficient, as well as the Nusselt number (Nu), increase monotonically with both nanoparticle volume concentration (α_p) and Reynolds number (Re). On the other hand, the addition of nanoparticles leads to an increase in viscosity. There is a controversial result concerning the empirical correlations for the Nu. Some experimental results indicated that the traditional correlations based on single-phase fluid cannot be applied to nanofluids, necessitating reconstruction of new correlations [2,3]. However, some results suggested that the traditional correlations for single-phase fluid remain valid for nanofluids, with the only requirement being the use of nanofluid-specific thermophysical properties [4,6].

Extensive numerical simulations have also been systematically employed to elucidate the fundamental flow and heat transfer characteristics of nanofluids. Four predominant computational approaches are commonly adopted: (i) the single-phase homogeneous model [7], (ii) the two-phase mixture model [8], (iii) the Eulerian–Eulerian multiphase model [9], and (iv) the Lagrangian discrete particle model [10]. The effectiveness of numerical simulation has been confirmed through the verification of experimental data. However, despite each numerical method achieving certain successes, none has been proven to possess an overwhelming advantage. Each numerical method has its own strengths and can meet different needs [11].

In contemporary engineering applications, advanced heat transfer media such as nanofluids are increasingly being adopted. Concurrently, researchers continue to pursue optimal heat exchanger designs and working fluid flow conditions. The aforementioned investigations primarily rely on the first law of thermodynamics (energy conservation principle) as their theoretical foundation. Although first-law analysis offers valuable insights into heat transfer efficiency, it falls short in identifying the optimal thermal operating conditions. Empirical studies confirm that while the enhanced thermal conductivity of nanofluids improves heat transfer, their increased viscosity can lead to counterproductive outcomes. However, first-law analysis cannot intuitively reveal the net effect of these competing factors. The second law of thermodynamics effectively bridges this gap through its entropy-based assessment framework.

Entropy generation analysis (EGA), which is grounded in the second law of thermodynamics, has emerged as a robust methodology for optimizing thermal transport processes. Several research groups have successfully applied EGA to study convective heat transfer characteristics of nanofluids in circular tube geometries. These studies can be systematically categorized into two distinct methodological approaches. The first approach adopts theoretical frameworks based on Bejan's seminal correlations for entropy generation rate [12]. The second approach directly computes entropy generation rates by leveraging velocity and temperature field data acquired from computational fluid dynamics (CFD) [13].

Singh et al. [14] theoretically analyzed Al_2O_3/water nanofluid flow and heat transfer in circular tubes using EGA. The study considered three tube diameters: microchannels (0.1 mm), minichannels (1 mm), and conventional channels (10 mm). Their results indicated that high-viscosity Al_2O_3/water nanofluids are unsuitable for conventional channels, highlighting the importance of developing low-viscosity nanofluids. Moghaddami et al. [15] also conducted a similar theoretical study and drew the conclusion that nanoparticle addition enhances efficiency mainly when heat transfer irreversibility dominates. Sohel et al. [16] evaluated entropy generation for various nanofluids in circular micro- and minichannels, comparing water-based and ethylene glycol-based systems. They found that water-based nanofluids exhibit lower entropy generation rates due to reduced heat transfer irreversibility, attributed to their higher thermal conductivity compared to ethylene glycol-based nanofluids. Bianco et al. [17] analytically explored entropy generation characteristics of nanofluids under three distinct inlet conditions: constant Reynolds number, fixed mass flow rate, and constant velocity. Mohseni-Gharyehsafa et al. [18] employed entropy generation minimization methodology to identify optimal parameters—such as nanoparticle volume fraction, Reynolds number, nanoparticle diameter, and average flow temperature—for turbulent nanofluid flow in circular tubes. Their findings

demonstrated that metallic oxide nanofluids (Al_2O_3 and CuO-based) generate significantly less entropy than nonmetallic oxide nanofluids (SiO_2-based). Mukherjee et al. [19] established a theoretical framework integrating genetic algorithms to optimize flow conditions for Al_2O_3-ethylene glycol nanofluids in circular tubes under constant wall temperature. Their optimized configuration included a mass flow rate of 0.54 kg/s, Reynolds number of 4000, nanoparticle diameter of 65 nm, and volume concentration of 0.2%.

The theoretical entropy generation analysis method, while useful, is largely constrained by empirical correlations and necessary simplifications, thus exhibiting applicability primarily to systems with simple geometric configurations and small wall–bulk temperature differences [20]. To overcome these limitations, researchers have increasingly adopted computational approaches that derive entropy generation rates directly from CFD simulations, thereby advancing nanofluid heat transfer optimization. Mwesigye and Huan [21] performed a thermodynamic analysis of turbulent forced convection in circular tubes by integrating EGA with CFD data. Their study covered tube cross-sectional areas ranging from 2.5×10^{-6} m^2 to 0.05 m^2, nanoparticle volume fractions from 0% to 6%, and Reynolds numbers between 5000 and 18,000. Their results showed that an optimal cross-sectional area exists for each Reynolds number, and that this optimal area increases with increasing Reynolds number. Ji et al. [22] applied CFD-based entropy generation analysis to investigate turbulent convective heat transfer characteristics of Al_2O_3/water nanofluids in circular tubes. Using a single-phase flow assumption, their study offered detailed insights into local entropy generation profiles. Rashidi et al. [23] conducted a systematic comparison between single-phase and two-phase modeling approaches for entropy generation analysis in TiO_2/water nanofluid forced convection. Their findings indicated identical entropy generation values for pure water across CFD approaches, while significant model discrepancies emerged with increasing nanoparticle volume fractions.

The accuracy of the turbulence model plays a crucial role in analyses that employ CFD to study the turbulent convective heat transfer of nanofluids. In previous studies, whether based on the first or second law of thermodynamics, the k-ε model has been the predominant choice [10,21,24,25], while the k-ω model has also been used in some studies [22,26]. These two-equation models rest on a theoretical framework that assumes homogeneous or weakly inhomogeneous turbulence. Yet, in near-wall regions characterized by strong inhomogeneity, their accuracy is often remains limited, even with the help of wall functions. To address this, various approaches have been proposed to extend such two-equation models to near-wall flows. One influential approach was introduced by Durbin [27], whose model captures near-wall turbulence behavior by solving an elliptic relaxation equation for the velocity-pressure gradient correlation tensor. This concept inspired a series of turbulence models, known as the $\overline{v}^2 - f$ models. To overcome the numerical challenges posed by the $\overline{v}^2 - f$ models, Manceau and Hanjalić [28] proposed the elliptic blending approach, greatly enhancing computational stability. Later, several research groups [29–31] further developed these elliptic-blending-based models and applied them to more complex configurations. Our research group had also developed a turbulence model (denoted as SST k-ω-φ-α model), which combines the elliptic-blending approach with the Shear Stress Transport (SST) formulation. By introducing an eddy viscosity modulation based on the turbulent specific rate and shear stress transport limitation, the proposed model not only preserves the benefits of elliptic-blending-based models for near-wall treatment, but also improves predictive accuracy in free shear layers. The model has been rigorously validated across several typical flow configurations, with results confirming its superiority over the k-ε and k-ω models [20,32,33].

To the best of the authors' knowledge, in existing numerical studies on turbulent flow and heat transfer of nanofluids, the turbulence models used are the k-ε model, k-ω model, and their variants, while turbulence models based on elliptic relaxation or elliptic blending methods have not yet been used. This study evaluates the performance of the in-house-developed elliptic blending turbulence model (the SST k-ω-φ-α model) for predicting the entropy generation in turbulent convective heat transfer of an Al_2O_3/water nanofluid

inside a circular tube under constant wall heat flux. The objectives are twofold: first, to validate the accuracy and demonstrate the superiority of the proposed turbulence model in predicting entropy generation during nanofluid heat transfer via numerical simulation; second, to provide guidance for extending the application of this turbulence model to entropy generation analysis in heat exchangers utilizing nanofluids, which typically feature more complex geometries and flow conditions.

The numerical modeling is elaborated in the following section. Results and discusions are presented in Sections 3 and 4, respectively, followed by a summary of the main conclusions in the final section.

2 Numerical Modeling

In this work, the two-phase mixture model was employed. The selection of the two-phase mixture model is primarily justified by its capability to capture the relative motion between phases (slip velocity) and non-uniform particle distribution, which are critical for accurately predicting nanofluid heat transfer. This model adopts a single-fluid approach, treating the nanofluid as a homogeneous mixture where the base fluid and nanoparticles are in thermal equilibrium and can interpenetrate, offering a balanced compromise between computational cost and physical fidelity. Here, the base fluid is defined as the primary phase, while the nanoparticles represent the secondary phase.

The following assumptions were incorporated into the numerical model:

(1) The mixture shares a common pressure field and a single temperature field, implying local thermal equilibrium.
(2) The influence of gravitational body force is neglected.
(3) The flow is steady, incompressible, and turbulent. Turbulence is modeled using the Reynolds-averaged Navier-Stokes (RANS) framework, with the Boussinesq hypothesis applied to relate the Reynolds stresses to the mean velocity gradients.
(4) The continuity, momentum, and energy equations are solved for the mixture as a whole. Additionally, a separate transport equation is solved for the volume fraction of the secondary phase.
(5) The turbulence model is applied to the mixture phase.

2.1 Governing Equations of Fluid Flow and Heat Transfer

2.1.1 Continuity Equation

The continuity equation for the mixture takes [34]

$$\nabla \cdot \left(\rho_m \vec{v}_m\right) = 0, \tag{1}$$

where ρ_m and $\vec{v}_m$ are the density and velocity vector of the mixture, respectively. They are determined using the following equations:

$$\rho_m = \sum_{q=1}^{N} \alpha_q \rho_q, \tag{2}$$

$$\vec{v}_m = \frac{\sum_{q=1}^{N} \alpha_q \rho_q \vec{v}_q}{\rho_m}, \tag{3}$$

where α_q, ρ_q and $\vec{v}_q$ are the volume fraction, density, and velocity vector of phase q, respectively, N is the total number of phases.

2.1.2 Momentum Equation

The momentum equation for the mixture can be written as [34]

$$\nabla \cdot \left(\rho_m \vec{v}_m \vec{v}_m\right) = -\nabla p + \nabla \cdot \left[\mu_m \left(\nabla \vec{v}_m + \nabla \vec{v}_m^T\right)\right] + \nabla \cdot \left(\sum_{k=1}^{N} \alpha_k \rho_k \vec{v}_{dr,k} \vec{v}_{dr,k}\right), \tag{4}$$

where p is the pressure. μ_m is the viscosity of the mixture and it can be written as

$$\mu_m = \mu_{l,m} + \mu_{t,m}, \tag{5}$$

in which $\mu_{l,m}$ and $\mu_{t,m}$ are the molecular viscosity and turbulent viscosity of the mixture, respectively. The $\mu_{t,m}$ is computed by the turbulence models, and the $\mu_{l,m}$ is computed as

$$\mu_{l,m} = \sum_{q=1}^{N} \alpha_q \mu_q, \tag{6}$$

where μ_q is the molecular viscosity of phase q. $\vec{v}_{dr,k}$ is the drift velocity for phase k and it is calculated by

$$\vec{v}_{dr,k} = \vec{v}_k - \vec{v}_m. \tag{7}$$

Introducing a relative (or slip) velocity,

$$\vec{v}_{kq} = \vec{v}_k - \vec{v}_q, \tag{8}$$

which represents the relative velocity of phase k to phase q, the drift velocity can be rewritten as

$$\vec{v}_{dr,k} = \vec{v}_{kq} - \frac{\sum_{i=1}^{N} \alpha_i \rho_i \vec{v}_{iq}}{\rho_m}. \tag{9}$$

In ANSYS Fluent, instead of Eq. (8), an algebraic formulation is used for the slip velocity, and it takes the form

$$\vec{v}_{kq} = \frac{\tau_k}{f_{drag}} \frac{\left(\rho_k - \rho_m\right)}{\rho_k} \vec{a}, \tag{10}$$

where ρ_k is the density of phase k, f_{drag} is the drag function, $\vec{a}$ is the acceleration vector. The τ_k is the particulate relaxation time, which is defined as

$$\tau_k = \frac{\rho_k d_k^2}{18 \mu_q}, \tag{11}$$

here d_k is the diameter of the particles.

For steady flow, when the effect of gravity is neglected, the acceleration vector can be expressed as

$$\vec{a} = -\left(\vec{v}_m \cdot \nabla\right) \vec{v}_m. \tag{12}$$

Many definitions for the drag function are available. In this work, the Schiller and Naumann model was used, and it is

$$f_{drag} = \begin{cases} 1 + 0.15 Re_r^{0.687} & Re_r \le 1000 \\ 0.0183 Re_r & Re_r > 1000 \end{cases}, \tag{13}$$

where Re_r is the relative Reynolds number, and it is defined as

$$\mathrm{Re}_r = \frac{\rho_q \left|\vec{v}_q - \vec{v}_k\right| d_k}{\mu_q}. \tag{14}$$

2.1.3 Energy Equation

The energy equation for the mixture can be written as [34]

$$\nabla \cdot \sum_{k=1}^{N} \alpha_k \rho_k c_{p,k} \vec{v}_k T_m = \nabla \cdot \left(\lambda_{\mathrm{eff}} \nabla T_m\right), \tag{15}$$

where $c_{p,k}$ is the specific heat of phase k, T_m is the temperature of the mixture, and λ_{eff} is the effective conductivity of the mixture calculated as

$$\lambda_{\mathrm{eff}} = \lambda_t + \sum_{k=1}^{N} \alpha_k \lambda_k, \tag{16}$$

where λ_k is the thermal conductivity of phase k, λ_t is the turbulent thermal conductivity of the mixture. The λ_t is calculated as

$$\lambda_t = \frac{c_{p,m} \mu_{t,m}}{\mathrm{Pr}_t}, \tag{17}$$

where $c_{p,m}$ is the specific heat of the mixture, and it is calculated using

$$c_{p,m} = \frac{\sum_{k=1}^{N} \alpha_k \rho_k c_{p,k}}{\rho_m}. \tag{18}$$

The turbulent Prandtl number was taken as $\mathrm{Pr}_t = 0.85$ in this work, following common practice in nanofluid forced-convection simulations [8,35,36].

2.1.4 Volume Fraction Equation for the Secondary Phase

In nanofluid flow, there is no mass transfer between the base fluid and nanoparticles. Consequently, the volume fraction equation for phase of the nanoparticles is

$$\nabla \cdot \left(\alpha_p \rho_p \vec{v}_m\right) = -\nabla \cdot \left(\alpha_p \rho_p \vec{v}_{dr,p}\right), \tag{19}$$

where $\vec{v}_{dr,p}$ is the drift velocity for the phase of nanoparticles [34].

2.2 Transport Equations of Turbulence Models

An in-house-developed elliptic blending turbulence model, specifically the SST k-ω-φ-α model, is employed for the mixture. The turbulent transport equations are presented below. These equations were rigorously formulated by replacing the variables of single-phase flow with their mixture counterparts, while preserving the constitutive relations and closure constants from the single-phase framework [32].

$$\nabla \cdot \left(\rho_m k_m \vec{v}_m\right) = G_{k,m} - \rho_m f_k \beta^* k_m \omega_m + \nabla \cdot \left[\left(\frac{\mu_m}{2} + \sigma_k \mu_{t,m}\right) \nabla k_m\right], \tag{20}$$

$$\nabla \cdot \left(\rho_m \omega_m \vec{v}_m\right) = f_\omega \gamma \frac{\omega_m}{k_m} G_{k,m} - \rho_m \beta \omega_m^2 + C_{D,m} + \nabla \cdot \left[\left(\frac{\mu_m}{2} + \sigma_\omega \mu_{t,m}\right) \nabla \omega_m\right], \tag{21}$$

$$\begin{aligned} \nabla \cdot \left(\rho_m \varphi_m \vec{v}_m\right) = {} & \left(1 - \alpha_m^p\right) \rho_m f_{\mathrm{wall},m} + \alpha_m^p \rho_m f_{\mathrm{hom},m} - \frac{\varphi_m}{k_m} G_{k,m} + \frac{2\sigma_k \mu_{t,m}}{k_m} \nabla \varphi_m \cdot \nabla k_m \\ & + \nabla \cdot \left[\left(\frac{\mu_m}{2} + \sigma_\varphi \mu_{t,m}\right) \nabla \varphi_m\right], \end{aligned} \tag{22}$$

$$0 = \frac{1-\alpha_m}{L_m^2} + \nabla \cdot \nabla \alpha_m. \tag{23}$$

The turbulent viscosity is calculated as

$$\mu_{t,m} = (1-\alpha^p)\, C_\mu \rho_m \varphi_m k_m \mathrm{Min}\left(T_m, T_{lim}\right) + \alpha^p \frac{a_1 \rho_m k_m}{\mathrm{Max}\left(a_1 \omega_m, F_2 S_m\right)}. \tag{24}$$

A comprehensive description of the SST k-ω-φ-α model is available in the work of Yang et al. [32].

For comparison, two industry-standard turbulence models—the realizable k-ε model and the SST k-ω model—were also employed. As these models are extensively documented in the ANSYS Fluent theory guide [34], their governing equations and closure coefficients are adopted directly from this source without restating here for brevity.

2.3 Formulas for Entropy Generations

The total local volumetric entropy generation rate, S'''_{gen}, in a viscous flow with convective heat transfer comprises two components: the rate due to friction irreversibility, $S'''_{gen,f}$, and the rate due to heat transfer irreversibility, $S'''_{gen,h}$. The relationship between them is given by

$$S'''_{gen} = S'''_{gen,f} + S'''_{gen,h}. \tag{25}$$

Generally, the $S'''_{gen,f}$ can be computed using either a direct or an indirect approach. Yang and Yang [20] demonstrated that, for the SST k-ω-φ-α turbulence model, the $S'''_{gen,f}$ should be computed via the indirect approach. While for the realizable k-ε model and the SST k-ω model, two approaches provide same results. Therefore, in this work, the indirect approach was adopted. In cylindrical coordinates, the components $S'''_{gen,f}$ and $S'''_{gen,h}$ can be calculated as follows [12,20]:

$$S'''_{gen,f} = \frac{\mu_{l,m} + \mu_{t,m}}{T_m} \left\{ 2\left[\left(\frac{\partial u_r}{\partial r}\right)^2 + \left(\frac{u_r}{r}\right)^2 + \left(\frac{\partial u_x}{\partial x}\right)^2 \right] + \left(\frac{\partial u_r}{\partial x} + \frac{\partial u_x}{\partial r}\right)^2 \right\} \tag{26}$$

$$S'''_{gen,h} = \frac{\lambda_{eff}}{T_m^2} \left[\left(\frac{\partial T_m}{\partial r}\right)^2 + \left(\frac{\partial T_m}{\partial x}\right)^2 \right]. \tag{27}$$

here, x and r denote the axial and radial coordinates, respectively. u_x and u_r represent the velocity components of the mixture in the axial and radial directions, respectively.

For flow in a circular tube, the entropy generation rate per unit length is obtained by integrating Eqs. (26) and (27) over the cross-section, yielding

$$S'_{gen,f} = \int_A S'''_{gen,f} dA, \tag{28}$$

and

$$S'_{gen,h} = \int_A S'''_{gen,h} dA. \tag{29}$$

2.4 Thermal Properties of Materials

The nanofluid considered in this work is composed of water as the base fluid and alumina (Al_2O_3) nanoparticles. Near ambient temperature, certain thermophysical properties—namely density, specific heat, and thermal conductivity—of both water and alumina exhibit minimal variation with temperature.

Therefore, they are treated as constants, and their values at T = 293.15 K, consistent with the operating temperature (20°C) in experiments of Pak and Cho [2], are listed in Table 1. In contrast, the viscosity of water exhibits a strong dependence on temperature. The functional relationship between the viscosity of water and temperature is

$$\mu_{bf} = 2.414 \times 10^{-5} \times 10^{\frac{247.8}{T-140.0}}. \tag{30}$$

where μ_{bf} is the dynamic viscosity of water, T is the temperature in Kelvin.

Table 1: Some thermal properties of the water and nanoparticles of Al_2O_3 at T = 293.15 K.

	Density, ρ (kg/m^3)	**Specific Heat, c_p (J/kg·K)**	**Thermal Conductivity, λ (W/m·K)**
Water	998.2	4183	0.599
Al_2O_3*	3880	773	36

Note: *Data from Pak and Cho [2].

The density and specific heat of the nanofluid are generally well-described by the classical relationships for a two-phase mixture, as given in Eqs. (2) and (18). In contrast, the dynamic viscosity and thermal conductivity do not follow the traditional rule of mixtures; therefore, specific correlations must be employed. In this study, the correlation between the dynamic viscosity ratio of the nanofluid to the base fluid and the nanoparticle volume fraction was derived using the experimental data reported by Pak and Cho [2] through a least-squares curve fitting approach. Their work measured the viscosity of Al_2O_3/water nanofluid at various nanoparticle volume concentrations under different shear rates ($\dot{\gamma}$). They found that the Al_2O_3/water nanofluid depicted the shear-thinning behaviour when $\alpha_p > 3\%$. In other words, the Al_2O_3/water nanofluid can be approximated to be Newtonian fluid when $\alpha_p < 3\%$. The experimantal data within the range of $\alpha_p = 0\%–4\%$ was selected for curve fitting. It shoud be noted that the datum at $\alpha_p = 4\%$ is based on high shear rate of $\dot{\gamma} = 384.1$ to ensure no abrupt changes. A comparison between the fitted curve and experimental data is presented in Fig. 1a, and the corresponding fitting expressions is as follow:

$$\frac{\mu_{nf}}{\mu_{bf}} = 1456.8\alpha_p^2 + 20.4\alpha_p + 1, \tag{31}$$

here μ_{nf} and μ_{bf} denote dynamic viscosities of the nanofluid and base fluid, respectively, and α_p represents the volume fraction of nanoparticles.

The correlation for the thermal conductivity ratio of nanofluid and base fluid, as a function of nanoparticle volume fraction, was established using the experimental data from Pak and Cho [2], originally measured by Masuda et al. [37]. A least-squares curve fitting method was applied to derive the relationship, and the resulting correlation is given by:

$$\frac{\lambda_{nf}}{\lambda_{bf}} = 7.61\alpha_p + 1, \tag{32}$$

where λ_{nf} and λ_{bf} are the thermal conductivities of nanofluid and base fluid, respectively. A comparison between the fitted curve and experimental data is presented in Fig. 1b.

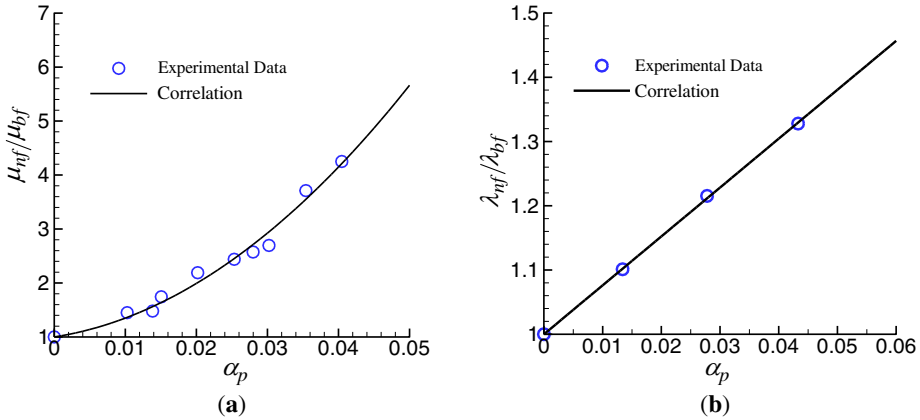

Figure 1: Experimental data and correlations for dynamic viscosity ratio and thermal conductivity ratio of nanofluid and base fluid. (**a**) dynamic viscosity ratio; (**b**) thermal conductivity ratio [2].

It should be noted that although the data provided in Pak and Cho [2] were obtained at a fixed temperature of 300 K, we consider the fitted correlation to remain valid across the temperature range considered in this study. This is supported by several experimental studies indicating that the thermal conductivity ratio is nearly independent of temperature [4,5]. Nevertheless, it is important to emphasize that the thermal conductivity of the base fluid itself does vary with temperature, and this should be taken into account when applying the proposed correlation.

It is important to note that the experimental data from Pak and Cho [2] obtained with nanoparticle concentrations ranging from 0% to 4.33% and temperatures between 293.15 and 345.65 K. Consequently, the applicable conditions for Eqs. (31) and (32) are confined to this range. If these bounds are substantially exceeded, the validity of the equations requires further assessment. In this study, the maximum nanoparticle concentration considered is 4%, and the highest temperature reaches 329.95 K, both of which fall within the applicable scope of the equations.

2.5 Model Implementation

The numerical simulations were conducted using the commercial software ANSYS Fluent (version 17.0). The transport equations for the in-house developed SST k-ω-φ-α turbulence model were implemented and solved through the User-Defined Scalar (UDS) functionality. Conversely, the SST k-ω and realizable k-ε models, available as built-in options in the software, were employed directly.

The system of governing equations includes the continuity, momentum, energy, volume fraction (for the secondary phase), and turbulence transport equations, which were solved using a pressure-based algorithm. The overall solution procedure is outlined in Fig. 2. Specifically, a pressure-based Coupled algorithm was used to solve the continuity and momentum equations simultaneously, while a pressure-based Segregated algorithm was employed to solve the volume fraction equation, the turbulence transport equations, and the energy equation sequentially.

Upon convergence, post-processing was performed to evaluate key parameters, including the Nusselt number, friction factor, heat transfer coefficient, and entropy generation rate.

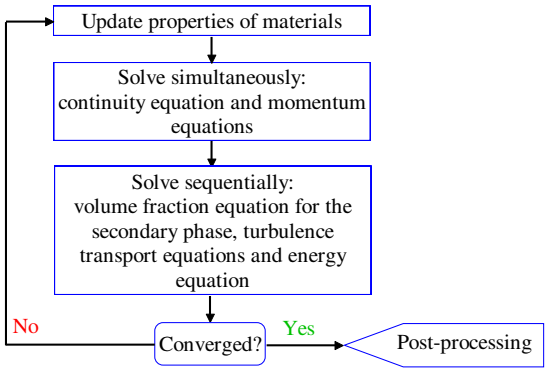

Figure 2: The solution procedure.

In this work, the diffusion terms in all governing equations were discretized using a central-differencing scheme. The convection terms in the continuity, momentum, energy, and turbulence equations were discretized with a second-order upwind scheme. For the convection term in the volume fraction equation, the QUICK scheme was applied. All derivatives and gradients were computed using the least-squares cell-based method.

2.6 Geometry and Boundary Conditions of the Computational Model

The problem under consideration involves a hydrodynamically fully developed, turbulent nanofluid flow in a circular tube. Owing to the geometric and physical axisymmetry of the problem, a two-dimensional axisymmetric model was adopted. The computational geometry and the corresponding boundary conditions are illustrated in Fig. 3. The computational domain comprises a hydrodynamic entry section ($-L_1 \le x < 0$) and a thermal section ($0 \le x < L_2$). The length of the hydrodynamic entry section was designed to be sufficient long to ensure that a fully developed turbulent flow would be established at the inlet ($x = 0$) of the thermal section.

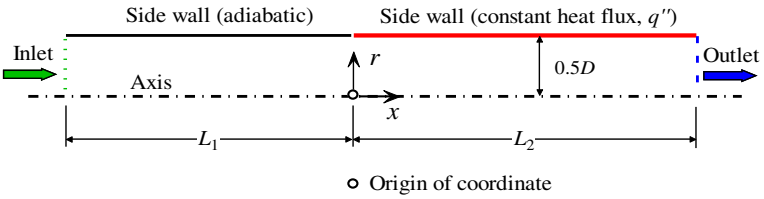

Figure 3: Geometry and boundary conditions of the computational model.

A static pressure of zero was imposed at the outlet. At the inlet, a uniform distribution was presumed for all physical quantities. The inlet values for velocity (u_{in}), temperature (T_{in}), turbulent kinetic energy (k_{in}), turbulent dissipation rate (ε_{in}), specific dissipation rate (ω_{in}), wall-normal turbulent anisotropy (φ_{in}) and elliptic variable (α_{in}) were specified as follows: $u_{in} = U_0$, $T_{in} = T_0$, $k_{in} = \frac{3}{2}(U_0 I)^2$, $\varepsilon_{in} = C_\mu \frac{\rho k_{in}^2}{\mu V_R}$, $\omega_{in} = \frac{\rho k_{in}}{\mu V_R}$, $\varphi_{in} = 0.4$, $\alpha_{in} = 1$. Here, U_0 and T_0 are the mean inlet velocity and temperature, respectively. In this work, the value of T_0 is 293.15 K, while $U_0 = \frac{\mu Re}{\rho D}$ is problem-dependent. I is the turbulence intensity, and V_R is the ratio of the turbulent viscosity to the molecular viscosity. Moreover, values of $I = 0.03$ and $V_R = 5$ were adopted. The constant $C_\mu = 0.09$ is a standard coefficient for the turbulence model.

The wall treatment method is determined by the specific turbulence model employed. For the SST k-ω-φ-α model, the following quantities were specified at the wall: $u_w = 0$, $k_w = 0$, $\omega_w = 3\nu/\left(\beta_0 y_1^2\right)$, $\varphi_w = 0$,

and $\alpha_w = 0$. Here, the subscript w denotes the wall value, ν is the kinematic viscosity of the nanofluid, y_1 is the normal distance from the centroid of the wall-adjacent cell to the wall, and $\beta_1 = 0.0708$ is a model constant [32]. The SST k-ω model utilized an automatic near-wall treatment for the wall boundary conditions [38], while the realizable k-ε model adopted the enhanced wall treatment method. A uniform heat flux was applied on the wall, with its specific value being problem-dependent.

2.7 Data Reduction

Upon achieving a converged solution, post-processing is performed. Key performance metrics, including the friction factor (f), Nusselt number (Nu), and entropy generation rate, are evaluated from the computed flow and temperature fields.

The friction factor is calculated using the following expression:

$$f = \frac{8\tau_w}{\rho U^2}, \tag{33}$$

where τ_w is the wall shear stress. The local Nusselt number on the wall can be evaluated by

$$\mathrm{Nu}(x) = \frac{h(x)D}{\lambda}, \tag{34}$$

where $h(x)$ is the heat transfer coefficient and it can be evaluated using

$$h(x) = \frac{q''}{T_w(x) - T_b(x)}, \tag{35}$$

and

$$T_b(x) = T_{in} + \frac{q''\pi Dx}{\dot{m}c_p}, \tag{36}$$

where x is the distance from the entrance of the thermal section, q'' is the heat flux per unit area, $\dot{m}$ is the mass flow rate, T_{in} is the temperature at inlet, T_w and T_b are the wall temperature and bulk mean temperature at cross-section, respectively.

The local volumetric entropy generation rates can be calculated using Eqs. (25)–(27), from which the entropy generation rates per unit length can be obtained via Eqs. (28) and (29).

For a fully developed, single-phase flow in a circular tube with constant fluid properties—an assumption that hold valid under small wall-bulk temperature difference condition—the friction factor, Nusselt number, and entropy generation rate per unit length can be evaluated using the following established correlations:

Petukhov's correlation [39]:

$$f = \left(0.790 \ln \mathrm{Re} - 1.64\right)^{-2} \left(3000 \le \mathrm{Re} \le 5 \times 10^6\right) \tag{37}$$

Gnielinski's correlation [39]:

$$\mathrm{Nu} = \frac{(f/8)\,(\mathrm{Re} - 1000)\,\mathrm{Pr}}{1 + 12.7\sqrt{f/8}\left(\mathrm{Pr}^{2/3} - 1\right)} \begin{pmatrix} 0.5 \le \mathrm{Pr} \le 2000 \\ 3000 \le \mathrm{Re} \le 5 \times 10^6 \end{pmatrix}. \tag{38}$$

Bejan's correlations [12]:

$$S'_{gen,h} = \frac{q'^2}{\pi \lambda T_b^2 Nu}, \tag{39}$$

and

$$S'_{gen,f} = \frac{32\dot{m}^3 f}{\pi \rho^2 T_b^2 D^5}. \tag{40}$$

where q' is the heat flux per unit length, D is the diameter of the tube.

In Eqs. (37)–(40), the thermophysical properties of the fluid are evaluated at the bulk mean temperature (T_b), defined as the arithmetic mean of the inlet temperature (T_{in}) and outlet temperature (T_{out}):

$$T_b = \frac{T_{in} + T_{out}}{2}. \tag{41}$$

However, when the wall-bulk temperature difference (ΔT) is too large to be neglected, Eq. (39) is no longer applicable. In such cases, the following alternative formulation should be employed [12,20]:

$$S'_{gen,h} = \frac{q' \Delta T}{T_b (T_b + \Delta T)}. \tag{42}$$

3 Results and Discussion

In all simulations performed in this study, the mean nanoparticle diameter was set to 13 nm, the tube diameter was D = 10.66 mm, and the tube length was $L_1 = L_2 = 100\,D$. Certain parameters were adjusted according to the specific case under investigation. For the studies presented in Sections 3.1 and 3.2, a constant heat flux of $q'' = 10,273\,W/m^2$ was applied, resulting in a small wall-bulk temperature difference [2]. A total of eight Reynolds numbers—10,000; 20,000; 30,000; 40,000; 50,000; 60,000; 80,000; and 100,000—were considered, all based on the fluid properties at the inlet of the thermal section. In Section 3.3, a substantially higher constant heat flux of $q'' = 500,000\,W/m^2$ was imposed, leading to a large wall-bulk temperature difference. Likewise, eight Reynolds numbers, calculated using the local properties at a specified streamwise location, were also examined. All subsequent analyses refer to the thermal section.

3.1 Verification and Validation

3.1.1 Mesh Independence Test

The computational domain was discretized using a mesh of quadrilateral cells. A grid refinement was applied in the near-wall region to accurately capture the steep gradients of variables. In the radial direction, the cell size increased progressively from the wall with a stretching ratio of 1.03, by contrast, a uniform grid distribution (the number of cells is 10,000) was adopted in the axial direction.

A grid independence study was conducted using four distinct mesh configurations to determine the optimal grid density. Simulations were performed for pure water flow and nanofluid ($\alpha_p = 0.04$) flow at Re = 100,000, with the key results summarized in Table 2. The results indicate that, both for the pure water flow and nanofluid flow, the 150-cell and 200-cell radial meshes yield outcomes in close agreement with the reference data. Considering the optimal trade-off between computational accuracy and cost, the configuration with 150 radial cells was selected for all subsequent simulations.

Table 2: **(a)** Results of mesh independence test (pure water); **(b)** results of mesh independence test ($\alpha_p = 0.04$).

The Number of Cells in the r-Direction	f	Nu	$S'_{gen,h}\left(\frac{W}{m \cdot K}\right)$	$S'_{gen,f}\left(\frac{W}{m \cdot K}\right)$
		(**a**)		
50	2.090×10^{-2}	735.0	0.279×10^{-3}	0.163
100	1.786×10^{-2}	613.6	1.125×10^{-3}	0.205
150	1.814×10^{-2}	590.0	1.227×10^{-3}	0.215
200	1.815×10^{-2}	590.7	1.225×10^{-3}	0.216
Ref.*	1.799×10^{-2}	598.4	1.223×10^{-3}	0.214
		(**b**)		
50	1.898×10^{-2}	796.2	8.0684×10^{-5}	4.8384
100	1.806×10^{-2}	884.5	6.0382×10^{-4}	6.8433
150	1.814×10^{-2}	821.2	6.6477×10^{-4}	6.9365
200	1.815×10^{-2}	822.5	6.6323×10^{-4}	6.9393
Ref.*	1.799×10^{-2}	845.3	6.5774×10^{-4}	6.8610

Note: *The reference data were calculated using Eqs. (37)–(40).

3.1.2 Model Validation

To validate the two-phase mixture model, numerical schemes, and thermophysical properties of the nanofluid, simulations were conducted on two cases with different nanoparticle volume fractions ($\alpha_p = 0.0134$ and $\alpha_p = 0.0278$). For comparison, each case was simulated using three different turbulence models.

Fig. 4 compares the numerically predicted heat transfer coefficient (h) at various Re with the experimental data reported by Pak and Cho [2]. At both $\alpha_p = 0.0278$ and $\alpha_p = 0.0134$, the SST k-ω-φ-α model shows excellent agreement with the experimental measurements. Both the SST k-ω model and the realizable k-ε model overpredict h, with the former exhibiting a more pronounced deviation.

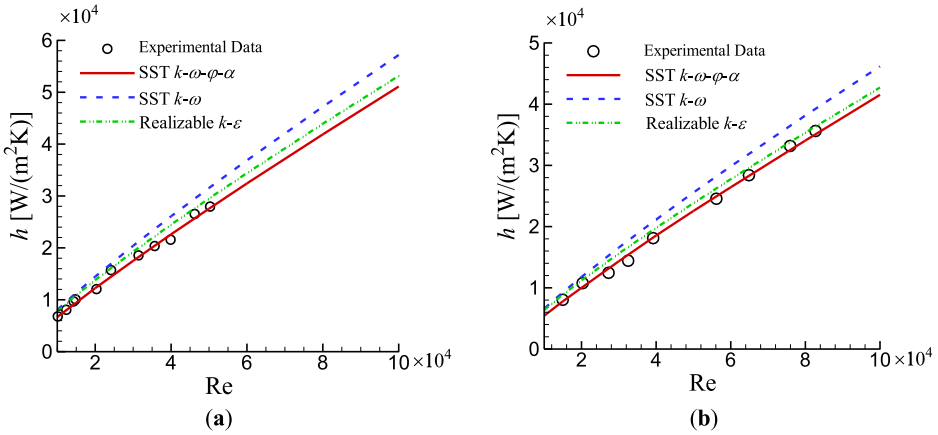

Figure 4: Comparison of the predicted heat transfer coefficient at various Re with experimental data [2]. (**a**) $\alpha_p = 0.0278$; (**b**) $\alpha_p = 0.0134$.

Fig. 5 compares the predicted friction factor (f) against values from Petukhov's correlation (Eq. (37)) across various Reynolds numbers. The predictions from the SST k-ω-φ-α model show excellent agreement with the correlation with a maximum discrepancy of approximately 1.87% at Re = 10,000. The SST k-ω model overpredicts the friction factor across all Reynolds numbers studied, with a maximum overprediction of about 3.88%. The realizable k-ε model exhibits a different behavior: it overestimates the friction factor at lower Reynolds numbers but underestimates it at higher Reynolds numbers, with a maximum deviation exceeding 7.48%.

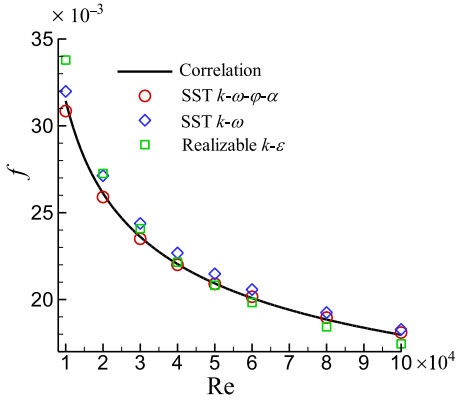

Figure 5: Comparison of the predicted friction factor with Petukhov's correlation (Eq. (37)) across various Re.

These results demonstrate that the SST k-ω-φ-α model accurately predicts both flow behavior (reflected by the friction factor in Fig. 5) and heat transfer performance (indicated by the heat transfer coefficient in Fig. 4) of nanofluids. As a result, the velocity and temperature fields obtained with this model offer a reliable foundation for evaluating the entropy generation rate. It should be noted that although we have not conducted direct validation of entropy generation based on experiments, the entropy generation calculated using Bejan's analytical formulation is feasible as long as the temperature and velocity fields are sufficiently accurate.

3.1.3 Computational Efficiency of the Turbulent Models

The SST k-ω-φ-α model has two more transport equations than the SST k-ω and realizable k-ε models, and need to handle more source terms, so that its computational cost will increase. We examined the computational efficiency of these three turbulence models for simulating of nanofluid flow. In the computational case, the number of computational cells is 1.5 million, the concentration of nanoparticles is 0.0278 and the Re is 100,000. The time consumed to calculate 100 steps based on the same hardware (52 CPU cores and 256 GB memory capacity) is recorded. To ensure statistical reliability, each turbulence model was simulated five times. The resulting CPU times were then averaged for each model. The time spent by the SST k-ω-φ-α model, the SST k-ω model and the realizable k-ε model is 96.9, 74.3 and 72.3 s, respectively. It can be seen that the time spent by the SST k-ω and realizable k-ε models is basically the same, while the time spent by the SST k-ω-φ-α model is larger, increasing by about 34% compared to the realizable k-ε model.

3.2 Entropy Generation Analysis under Small Wall-Bulk Temperature Difference Condition

3.2.1 Profiles of the Entropy Generation Rate on Cross-Section

Analyzing the radial distribution of the local entropy generation rate offers detailed insights into the spatial variation of entropy generation across the flow field. Decomposing the total entropy generation

rate into its components—contributions from friction irreversibility ($S'''_{gen,f}$) and heat transfer irreversibility ($S'''_{gen,h}$)—is essential for understanding their respective contributions. In this subsection, the case with $\alpha_p = 0.0278$ is selected as representative example for analysis.

Due to the small wall-bulk temperature difference, the thermophysical properties of the nanofluid can be regarded as constants. Moreover, as the flow is hydrodynamically fully developed and turbulent at the entrance of the thermal section, this flow state remain unchanged along the entire length. According to Eq. (26), the entropy generation rate due to friction irreversibility, $S'''_{gen,f}$, depends solely on the velocity field; thus, its radial distribution is identical at every cross-section. Given the similarity of results across different Reynolds numbers, only the case at Re = 10,000 is presented here.

Fig. 6 shows the radial profiles of $S'''_{gen,f}$, predicted by the three turbulence models. Since $S'''_{gen,f}$ is predominantly generated in the thin near-wall region, the wall-normal distance is normalized by $y^+ = \rho u_\tau y/\mu$ and used as the abscissa for clarity, where $u_\tau = \sqrt{\tau_w/\rho}$ is the friction velocity and y is the distance from the wall. The peak value of $S'''_{gen,f}$ occurs at the wall, which aligns with the position of the maximum velocity gradient. Most of the $S'''_{gen,f}$ is generated within the viscous sublayer ($y^+ < 5$) and the buffer layer ($5 \le y^+ < 30$). In addition, discrepancies among the predictions of the three turbulence models are primarily confined to the viscous sublayer. The realizable k-ε model predicts the highest value, while the SST k-ω-φ-α model gives the lowest. This difference mainly results from the different near-wall treatments adopted by the models and their varying accuracy in resolving the near-wall flow physics.

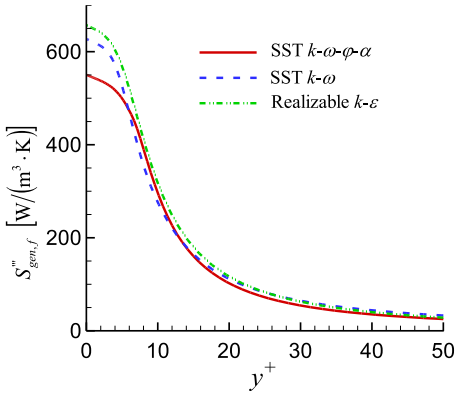

Figure 6: Profiles of entropy generation rate due to friction irreversibility on the cross-section predicted by different turbulence models.

After the hydrodynamically fully developed turbulent flow enters the thermal section, it passes through a short thermal entrance region (approximately < 10D [39]) before achieving a thermally fully developed state. Within this thermal entrance region, the profile of $S'''_{gen,h}$ evolves axially, driven by the developing temperature field.

Fig. 7 depicts the evolution of the $S'''_{gen,h}$ profiles predicted by the SST k-ω-φ-α model at various axial locations (x/D) for the case of Re = 10,000. It can be observed that beyond x/D > 5, the profiles remain nearly unchanged with further axial progression. This confirms that the thermal entrance length is short compared to the total length of the thermal section under consideration. Additionally, it is well established that the thermal entrance length decreases with increasing Reynolds number. Therefore, when averaging $S'''_{gen,h}$ over the entire thermal section, the influence of the entrance region is limited, and the associated error is negligible.

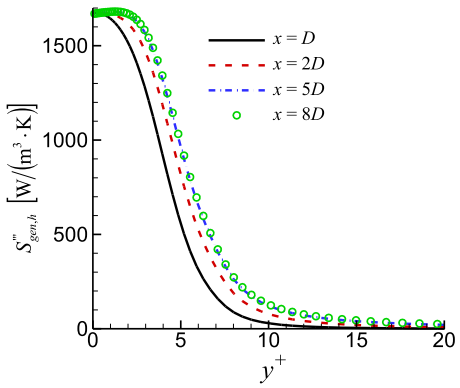

Figure 7: Profiles of entropy generation rate due to heat transfer irreversibility at different x-position.

As indicated by Eq. (27), the entropy generation rate due to heat transfer irreversibility, $S'''_{gen,h}$, depends exclusively on the temperature gradient. For a thermally fully developed flow with constant thermophysical properties under a constant heat flux boundary condition, the temperature gradient profile—and consequently, the profile of $S'''_{gen,h}$—remains unchanged along the axial direction.

Fig. 8 compares the radial profiles of $S'''_{gen,h}$ at the axial location of x/D = 50, predicted by different turbulence models. The peak value of $S'''_{gen,h}$ occurs at the wall, which corresponds to the position of the maximum temperature gradient. The majority of $S'''_{gen,h}$ is generated within the viscous sublayer ($y^+ < 5$) and the inner part of the buffer layer ($5 \leq y^+ < 10$). Discrepancies among the predictions by different turbulence models are primarily confined to this near-wall region. Notably, the region of significant $S'''_{gen,h}$ predicted by the SST k-ω-φ-α model is more extensive than those predicted by the other two models. The difference between the results from the SST k-ω model and the realizable k-ε model is relatively minor.

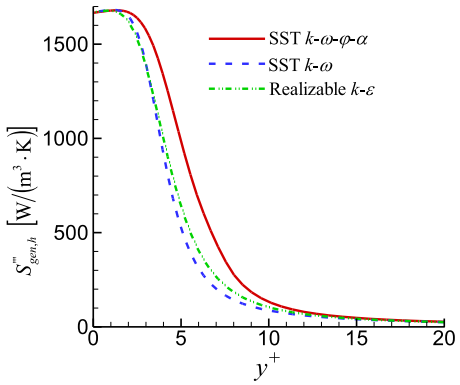

Figure 8: Profiles of entropy generation rate due to heat transfer irreversibility on the cross-section at x/D = 50 predicted by different turbulence models.

3.2.2 The Entropy Generation Rate per Unit Length

For flow in a circular tube, the entropy generation rates per unit length due to friction ($S'_{gen,f}$) and heat transfer ($S'_{gen,h}$) are obtained by integrating their respective local volumetric rates ($S'''_{gen,f}$ and $S'''_{gen,h}$) over the cross-section within the thermal section, as defined by Eqs. (28) and (29). In this subsection, the integration is performed at a fixed axial location of x/D = 50. The resulting values for $S'_{gen,h}$ and $S'_{gen,f}$ are thus directly comparable to the corresponding Bejan's correlations of Eqs. (39) and (40), respectively.

Fig. 9 compares the entropy generation rate per unit length due to heat transfer irreversibility ($S'_{gen,h}$), as predicted by different turbulence models, against the correlation given by Eq. (39). The Re range considered in this comparison is from 10^4 to 10^5. It is evident that $S'_{gen,h}$ decreases with increasing Re.

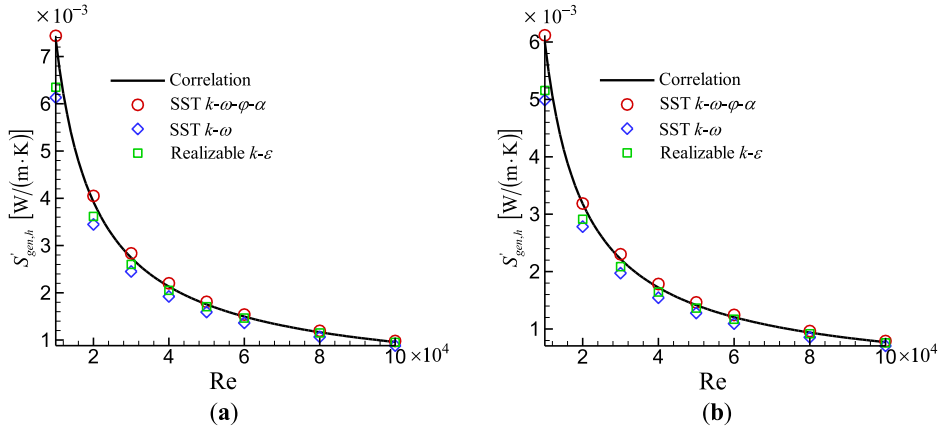

Figure 9: Comparisons of the entropy generation rate per unit length due to heat transfer irreversibility $S'_{gen,h}$ predicted by different turbulence models with correlation (Eq. (39)): (**a**) α_p = 0.0134; (**b**) α_p = 0.0278.

Upon quantitative examination of the data, we found that the maximum deviation of the SST k-ω-φ-α model from Bejan's correlation occurs at Re = 30,000, whereas for the other two models, it occurs at Re = 10,000. The specific values are listed in Table 3. Notably, the predictions of the SST k-ω-φ-α model exhibit good agreement with Bejan's correlation. The maximum deviation of this model is only 3.36% for the case of α_p = 0.0134 and 3.75% for the case of α_p = 0.0278. In contrast, both the SST k-ω model and the realizable k-ε model consistently underpredict $S'_{gen,h}$ across the entire Reynolds number range. For the SST k-ω model, the maximum deviation exceeds 16.74% (for α_p = 0.0134) and 16.82% (for α_p = 0.0278). Similarly, the realizable k-ε model shows maximum deviations exceeding 13.78% (for α_p = 0.0134) and 14.03% (for α_p = 0.0278).

Table 3: The deviations of predicted $S'_{gen,h}$ compared with Bejan's correlation.

Re	Turbulence Models	α_p = 0.0134		α_p = 0.0278	
		$S'_{gen,h}$ (W/(m·K))	Deviation (%)	$S'_{gen,h}$ (W/(m·K))	Deviation (%)
10,000	Reference data*	7.3639×10^{-3}	—	5.9973×10^{-3}	—
	SST k-ω-φ-α	7.4380×10^{-3}	1.00	6.1172×10^{-3}	2.00
	SST k-ω	6.1314×10^{-3}	16.74	4.9886×10^{-3}	16.82
	Realizable k-ε	6.3495×10^{-3}	13.78	5.1558×10^{-3}	14.03
30,000	Reference data*	2.7422×10^{-3}	—	2.2189×10^{-3}	—
	SST k-ω-φ-α	2.8343×10^{-3}	3.36	2.3021×10^{-3}	3.75
	SST k-ω	2.4511×10^{-3}	10.62	1.9733×10^{-3}	11.07
	Realizable k-ε	2.5997×10^{-3}	5.19	2.0864×10^{-3}	5.97

Note: *The reference data were obtained from Bejan's correlation (Eq. (39)).

Fig. 10 compares the entropy generation rate per unit length due to friction irreversibility ($S'_{gen,f}$), predicted by different turbulence models, against Bejan's correlation given in Eq. (40). The variation trend of $S'_{gen,f}$ with Re is opposite to that of $S'_{gen,h}$. Specifically, $S'_{gen,f}$ increases with increasing Re.

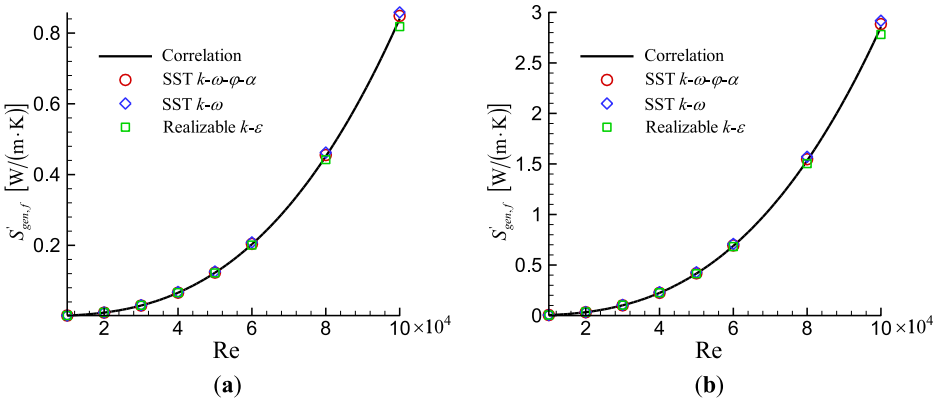

Figure 10: Comparisons of the entropy generation rate per unit length due to friction irreversibility $S'_{gen,f}$ predicted by different turbulence models with correlation (Eq. (40)): (**a**) $\alpha_p = 0.0134$; (**b**) $\alpha_p = 0.0278$.

The maximum deviations of predicted $S'_{gen,f}$ compared to Bejan's correlation occur at Re = 10,000 for all three turbulence models, as listed in Table 4. Consistent with the previous findings, the predictions of the SST k-ω-φ-α model for $S'_{gen,f}$ also show good agreement with Bejan's correlation. The maximum deviations of this model are only 1.40% for the case of $\alpha_p = 0.0134$ and 1.85% for the case of $\alpha_p = 0.0278$. In contrast, the results from both the SST k-ω model and the realizable k-ε model exhibit larger deviations from Bejan's correlation. For the realizable k-ε model, the maximum deviations exceed 7.99% (for $\alpha_p = 0.0134$) and 7.54% (for $\alpha_p = 0.0278$). The predictions of the SST k-ω model are, however, slightly more accurate than those of the realizable k-ε model, with maximum deviations of 5.74% (for $\alpha_p = 0.0134$) and 5.16% (for $\alpha_p = 0.0278$).

Table 4: The deviations of predicted $S'_{gen,f}$ compared with Bejan's correlation at Re = 10,000.

Re	Turbulence Models	$\alpha_p = 0.0134$		$\alpha_p = 0.0278$	
		$S'_{gen,f}$ (W/(m·K))	Deviation (%)	$S'_{gen,f}$ (W/(m·K))	Deviation (%)
10,000	Reference data*	1.4704×10^{-3}	—	4.9958×10^{-3}	—
	SST k-ω-φ-α	1.4498×10^{-3}	1.40	4.9030×10^{-3}	1.85
	SST k-ω	1.5548×10^{-3}	5.74	5.2538×10^{-3}	5.16
	Realizable k-ε	1.5879×10^{-3}	7.99	5.3728×10^{-3}	7.55

Note: *The reference data were obtained from Bejan's correlation (Eq. (40)).

The results presented above confirm that, under condition of a small wall-bulk temperature difference, the Bejan's correlations for entropy generation rate—originally developed for single-phase flow—remain valid for nanofluids, provided that the nanofluid-specific thermophysical properties are used in the calculations. The results also demonstrate that the SST k-ω-φ-α model accurately predicts the entropy generation rate for nanofluid flow in a circular tube under a constant heat flux boundary condition. This accuracy is primarily attributed to the model's enhanced capability in resolving the velocity and temperature fields in the near-wall region [32]. In contrast, the predictions from both the SST k-ω model and the realizable k-ε model show significant deviations from the correlations for the entropy generation rate due to heat

transfer irreversibility ($S'_{gen,h}$). For the friction component ($S'_{gen,f}$), however, the deviations of both models fall within an acceptable range. Therefore, for accurate simulation of nanofluid flow and heat transfer in circular tubes and the consequent precise calculation of entropy generation, the SST k-ω-φ-α model is highly recommended.

3.2.3 The Effect of Nanoparticle Volume Fraction on Entropy Generation Rate

The nanoparticle volume fraction (α_p) exerts a significant influence on the thermophysical properties of nanofluids, particularly the dynamic viscosity and thermal conductivity (see Eqs. (31) and (32)). Furthermore, these properties govern the flow and heat transfer characteristics in the near-wall region, thereby directly affecting the entropy generation rates. The effect of α_p on the entropy generation rates was evaluated using the SST k-ω-φ-α model, with the results being presented in Fig. 11. Three nanoparticle volume fractions (α_p = 0.0134, 0.0278 and 0.04) and eight Reynolds numbers (ranging from 10^4 to 10^5) were considered. The curves in Fig. 11 were obtained by fitting the numerical data.

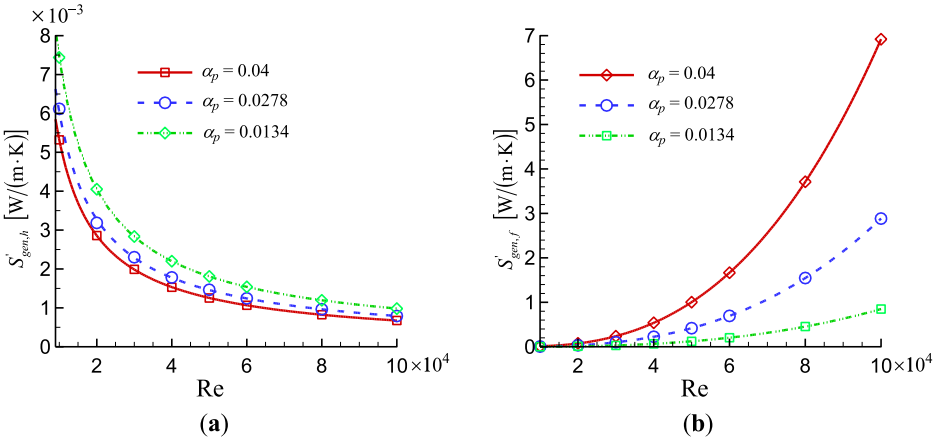

Figure 11: The effect of the volume fraction of the nanoparticles on the entropy generation rates. (**a**) $S'_{gen,h}$; (**b**) $S'_{gen,f}$.

The results show that as α_p increases, the entropy generation rate due to heat transfer irreversibility ($S'_{gen,h}$) decreases slightly, while the rate due to friction irreversibility ($S'_{gen,f}$) increases substantially. To elucidate this trend, we examine the underlying physical mechanisms. As illustrated in Fig. 1, both the dynamic viscosity and thermal conductivity of the nanofluid increase with α_p. According to Eq. (39), $S'_{gen,h}$ is inversely proportional to thermal conductivity when the Reynolds number and other parameters hold constant. Therefore, an increase in α_p, which enhances thermal conductivity, leads to a reduction in $S'_{gen,h}$. On the other hand, an increase in dynamic viscosity requires a higher flow velocity—and consequently a higher mass flow rate ($\dot{m}$)—to maintain a constant Reynolds number. Eq. (40) shows that $S'_{gen,f}$ is proportional to the cube of the mass flow rate ($\dot{m}^3$) when other parameters are constant. As a result, $S'_{gen,f}$ rises markedly with increasing α_p.

It is also noteworthy that the entropy generation rate due to friction irreversibility ($S'_{gen,f}$) is approximately three orders of magnitude greater than that due to heat transfer irreversibility ($S'_{gen,h}$), implying that the total entropy generation rate is primarily governed by the friction component ($S'_{gen,f}$). Therefore, increasing the nanoparticle volume fraction (α_p) imposes an overall adverse effect on the thermodynamic performance of the heat transfer process, owing to a significant increase in total irreversibility. This finding is consistent with the conclusion of Singh et al. [14], who argued that high-viscosity Al_2O_3/water

nanofluids are unsuitable for conventional channel flows and emphasized the importance of developing low-viscosity nanofluids.

3.3 Entropy Generation Analysis under Large Wall-Bulk Temperature Difference Condition

In this section, a constant wall heat flux of $q'' = 500,000\ W/m^2$ was applied, resulting in a substantial wall-bulk temperature difference. Under this condition, the thermophysical properties of the nanofluid, particularly the dynamic viscosity, become spatially non-uniform and exhibit strong temperature dependence. While one nanoparticle volume fraction of $\alpha_p = 0.0278$ was considered in Sections 3.3.1 and 3.3.2, three different nanoparticle volume fractions ($\alpha_p = 0.0134, 0.0278, 0.04$) were considered in Section 3.3.3.

A critical issue under such circumstances is the selection of an appropriate reference temperature for evaluating the nanofluid properties required to compute parameters such as Nu, Re, and f. In the subsequent analysis, the specific reference temperature and its corresponding axial position used in the property evaluation are clearly stated in each respective subsection.

3.3.1 The Integrals of Entropy Generation Rate on Various Cross-Sections

In this subsection, the Re is calculated based on the nanofluid properties at the inlet of the thermal section, with a temperature of 293.15 K. Similar to the cases with small wall-bulk temperature differences, the local volumetric entropy generation rate is highest in the near-wall region. A key difference, however, is that the entropy generation rates per unit length, which are obtained by integrating across different cross-sections, do not remain constant along the axial direction of the tube.

Fig. 12 shows the axial variations of the entropy generation rates per unit length due to friction ($S'_{gen,f}$) and heat transfer ($S'_{gen,h}$). Given the similarity of results at various Re, we analyze only two representative cases: Re = 10,000 and Re = 100,000. As shown in Fig. 12a,b, $S'_{gen,f}$ decreases monotonically along the axial direction. However, $S'_{gen,h}$ exhibits a non-monotonic trend, initially increasing and then decreasing along the tube axis (Fig. 12c,d).

Although the qualitative trends for both $S'_{gen,f}$ and $S'_{gen,h}$ are consistent across different Reynolds numbers, the magnitude of the axial variation—quantified by the difference between the maximum and minimum values—varies with the Reynolds number. As shown in Fig. 12a,c, at a low Reynolds number (Re = 10,000), the relative change in both $S'_{gen,f}$ and $S'_{gen,h}$ between the inlet and outlet exceeds 10%. In contrast, at a high Reynolds number (Re = 100,000), the relative change is less pronounced, remaining below 5% (Fig. 12b,d).

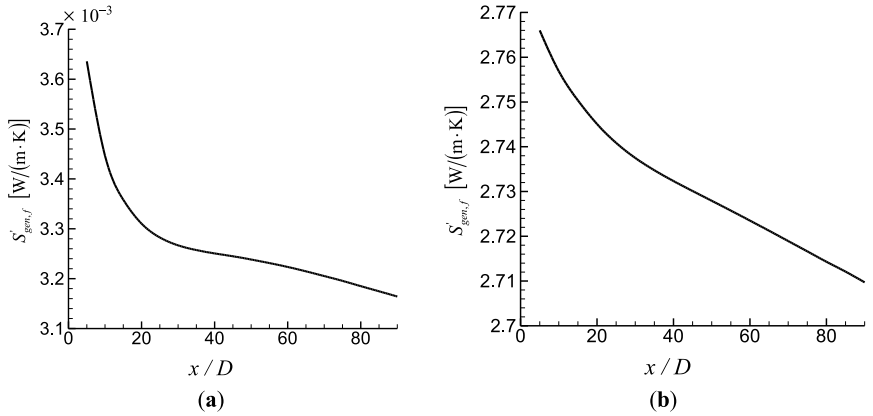

Figure 12: (Continued)

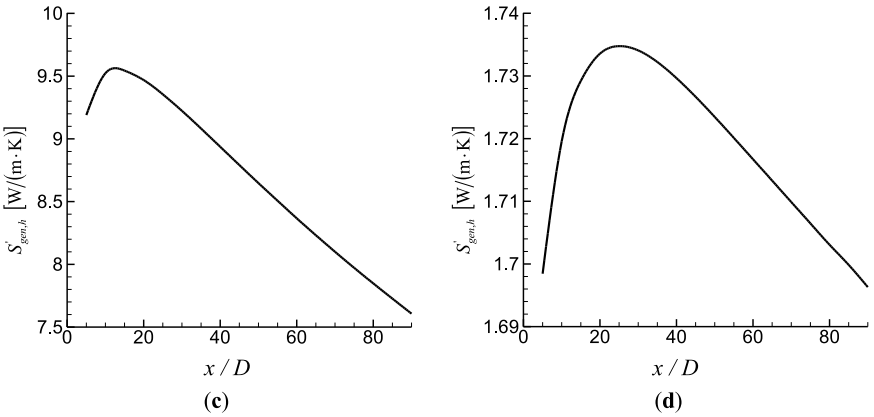

Figure 12: The integrals of entropy generation rate on various cross sections. (**a**) $S'_{gen,f}$, Re = 10,000; (**b**) $S'_{gen,f}$, Re = 100,000; (**c**) $S'_{gen,h}$, Re = 10,000; (**d**) $S'_{gen,h}$, Re = 100,000.

3.3.2 The Entropy Generation Rate per Unit Length

This subsection focuses on the results at the axial location of x/D = 50. Accordingly, unless otherwise specified, the thermophysical properties of the nanofluid are evaluated at the bulk mean temperature of this cross-section. Under this condition, the range of Re considered here is 13,188 to 102,877.

As previously indicated, a significant wall-bulk temperature difference renders Bejan's correlation (Eq. (39)) inadequate for accurately evaluating the entropy generation rate due to heat transfer irreversibility ($S'_{gen,h}$). Instead, Eq. (42) should be employed. In addition, the applicability of Eq. (40) for predicting the entropy generation rate due to friction irreversibility ($S'_{gen,f}$) under such large wall-bulk temperature differences must also be re-examined.

Fig. 13 compares the entropy generation rate per unit length ($S'_{gen,h}$ and $S'_{gen,f}$) obtained from different methods. The solid line denotes the results from the present numerical simulations. In Fig. 13a, the dashed and dash-dot-dot lines represent the values computed using Eq. (42) and Bejan's correlation (Eq. (39)), respectively. In Fig. 13b, the dash-dot-dot line depicts the results from Bejan's correlation (Eq. (40)), wherein the friction factor (f) is evaluated using Petukhov's correlation (Eq. (37)).

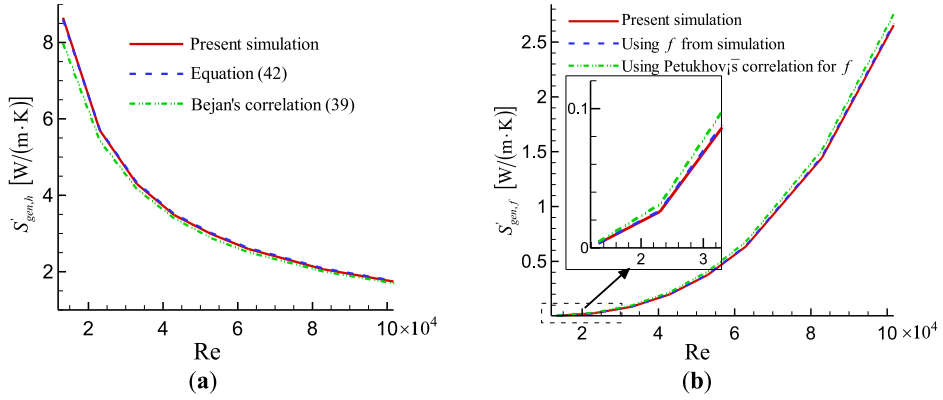

Figure 13: The entropy generation rate per unit length at x/D = 50. (**a**) $S'_{gen,h}$; (**b**) $S'_{gen,f}$.

It can be seen from Fig. 13a that the simulation results of $S'_{gen,h}$ agree excellently with Eq. (42) across all Reynolds numbers but show slight deviations from Bejan's correlation (Eq. (39)). A maximum deviation

of 7.3% occurs at the lowest Re of 13,188. The deviation gradually decreases with increasing Re. This trend is directly attributed to the reduction in the wall-bulk temperature difference with increasing Re. For instance, the temperature difference decreases from 56.8 K at Re = 13,188 to merely 9.3 K at Re = 102,877. It can be expected that when the temperature difference narrows to a negligible level, the difference between Eqs. (39) and (42) will disappear.

For $S'_{gen,f}$ in Fig. 13b, a pronounced deviation is observed between our numerical results and the predictions from the combination of Bejan's and Petukhov's correlations. Similarly, the maximum deviation, exceeding 37.5%, occurs at Re = 13,188. The deviation gradually decreases with increasing Re. This significant discrepancy is primarily traced to an inaccurate evaluation of the friction factor (f). In Petukhov's correlation, the Re is calculated using the nanofluid viscosity evaluated at the bulk temperature. However, the friction factor is predominantly governed by the nanofluid viscosity in the near-wall region, which is affected strongly by the wall temperature. Consequently, a large wall-bulk temperature difference thus introduces considerable error in the predicted friction factor.

Fig. 14 compares the friction factors from different evaluation methods. Evidently, the friction factor evaluated at the wall temperature agrees well with the simulation results, whereas the value based on the bulk temperature shows a considerable deviation. The deviation decreases with increasing Re, consistent with the reducing wall-bulk temperature difference. Substituting the numerically obtained friction factors into Bejan's correlation—replacing Petukhov's correlation (Eq. (37))—yields a significantly improved agreement, as shown by the dashed line in Fig. 13b. This correction reduces the maximum deviation to 5.6%.

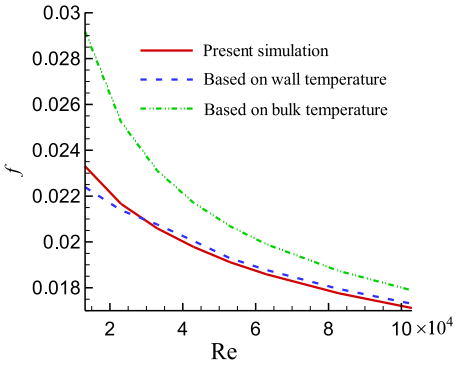

Figure 14: The friction factors obtained by different methods.

In summary, the analysis in this subsection demonstrates that Bejan's correlations are not applicable for predicting both entropy generation rate due to heat transfer ($S'_{gen,h}$) and that due to friction ($S'_{gen,f}$) under significant wall-bulk temperature difference. Under this condition, accurate prediction must rely on the fundamental definitions of local volumetric entropy generation rates for heat transfer (Eq. (27)) and friction (Eq. (26)). These definitions, in turn, require highly accurate velocity and temperature fields as inputs. Consequently, high-fidelity numerical simulations, supported by accurate, robust, and reliable turbulence models, become essential.

3.3.3 The Effect of Nanoparticle Volume Fraction on Entropy Generation Rate

This subsection examines the influence of the nanoparticle volume fraction (α_p) on the entropy generation rate using the SST k-ω-φ-α model. Three values of nanoparticle volume fractions (α_p = 0.0134, 0.0278, and 0.04) were considered, along with eight Reynolds numbers ranging from 10^4 to 10^5. It is noted that the Reynolds number was evaluated based on the nanofluid properties at the inlet of the thermal section. The

entropy generation rate per unit length at the axial location of x/D = 50 was selected for analysis. Numerical results were fitted into smooth curves via the least-squares method and are presented in Fig. 15.

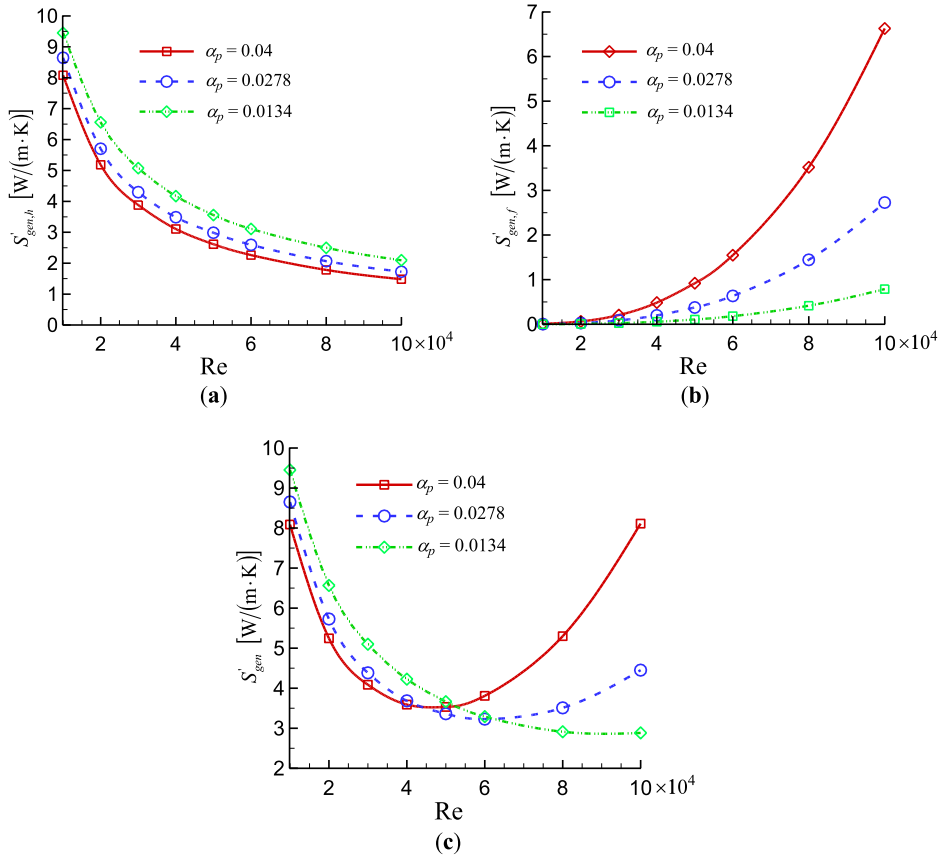

Figure 15: The effect of the volume fraction of the nanoparticles on the entropy generation rate. (**a**) $S'_{gen,h}$; (**b**) $S'_{gen,f}$; (**c**) S'_{gen}.

Under a large wall-bulk temperature difference, the trends of the entropy generation rates per unit length due to heat transfer ($S'_{gen,h}$) and friction ($S'_{gen,f}$) with respect to the nanoparticle volume fraction (α_p) are similar to those observed under a small wall-bulk temperature difference (see Section 3.2.3). Specifically, as α_p increases, $S'_{gen,h}$ decreases slightly (Fig. 15a), whereas $S'_{gen,f}$ increases substantially (Fig. 15b).

Notably, the total entropy generation rate per unit length (S'_{gen}) deserves particular attention. Unlike the case with a small wall-bulk temperature difference, a large wall-bulk temperature difference can result in $S'_{gen,h}$ and $S'_{gen,f}$ being of the same order of magnitude. Consequently, the thermodynamic performance of the heat transfer process should be assessed based on the total entropy generation rate (S'_{gen}) rather than on either individual component alone.

Fig. 15c shows the variation of S'_{gen} (sum of $S'_{gen,h}$ and $S'_{gen,f}$) with Re. Due to the fact that $S'_{gen,h}$ decreases with increasing Re, while $S'_{gen,f}$ increases with increasing Re, and they are of the same order of magnitude, so S'_{gen} decreases first and then increases with increasing Re. This trend indicates that for each value of α_p, there exists an optimal Re that minimizes the total entropy generation rate. Moreover, at lower Re, S'_{gen} decreases as α_p increases, suggesting that a higher α_p improves thermodynamic performance. Conversely, at higher Re, S'_{gen} increases with α_p, implying that raising α_p adversely affects thermodynamic performance.

Figs. 11 and 15 illustrate the variations of entropy generation rates due to friction and heat transfer irreversibilities. While dimensionless parameter (such as the Bejan number) is commonly used to identify the dominant mechanism, the present study emphasizes the order-of-magnitude analysis of dimensional entropy generation rates. This approach is adopted because it provides a direct measure of the absolute thermodynamic loss in the system. For complex nanofluid flows where thermophysical properties vary significantly, understanding the absolute scales of friction and heat transfer irreversibilities is more critical for engineering design than relying solely on normalized ratios.

4 Discussion

This study demonstrated that high-fidelity simulation, supported by advanced turbulence models capable of accurately capturing near-wall turbulence behavior, is crucial for reliably designing and optimizing nanofluid-based heat exchange systems. It clarified the trade-off between heat transfer enhancement and increased irreversibility, offering guidance for future development and applications of nanofluids. The study also provides some guidance on the considerations of applying the elliptic blending turbulence model to more complex geometric configurations and flow conditions [40,41].

This work is limited to the application of the SST k-ω-φ-α model to Al_2O_3/water nanofluid in simple geometry. The high accuracy achieved in simulating single-phase flow for complex configurations—such as separated flow, backward-facing step flow, and impinging jet flow—confirms the robustness of the proposed turbulence model [32]. Furthermore, since the model does not rely on specific nanofluid formulations, it is highly scalable. By incorporating appropriate correlations for the effective thermophysical properties of nanofluids, the method can be seamlessly extended to investigate the hydrothermal performance of various nanofluids flowing through arbitrarily complex geometries.

It is worth noting that while the present model treats nanoparticles as ideal spheres within a Newtonian base fluid, real nanofluids often exhibit more complex behaviors. In practical applications, nanoparticles may deviate significantly from perfect sphericity, and the suspending fluid can display non-Newtonian shear-thinning [2,42], particularly at high volume fractions. Furthermore, the heat transfer enhancement mechanisms in nanofluids are intrinsically linked to micro-scale phenomena, specifically Brownian motion and thermophoresis, which induce particle migration and non-uniform distributions that are not captured by the homogeneous two-phase assumption.

Moreover, certain limitations inherent to the mixture model employed in this study must be acknowledged. The model assumes a single turbulence field shared by both phases, which may oversimplify the physics at high Reynolds numbers; specifically, the dispersed nanoparticles likely possess a distinct turbulence structure and experience different levels of turbulent dispersion compared to the carrier fluid. Furthermore, under large temperature gradients, thermophoresis becomes significant. While the mixture model incorporates a drift velocity to account for this effect, it relies on empirical correlations for the thermophoretic force that may not be universally valid across all nanoparticle morphologies and sizes.

5 Conclusion

This study conducted a comprehensive numerical investigation into the turbulent convective heat transfer and entropy generation characteristics of Al_2O_3/water nanofluid flow in a circular tube under a constant heat flux boundary condition. The primary objective was to evaluate the performance of an in-house developed elliptic blending turbulence model (SST k-ω-φ-α) against industry-standard models and to analyze the thermodynamic performance through detailed entropy generation analysis. The main conclusions are summarized as follows:

(1) The SST k-ω-φ-α model delivers superior accuracy in predicting both fluid flow (friction factor) and heat transfer (heat transfer coefficient) of nanofluids. Its predictions align closely with established experimental data and empirical correlations, outperforming the SST k-ω and realizable k-ε models. This improvement stems from the model's enhanced resolution of near-wall flow physics, which is essential for accurately predicting the entropy generation rate.

(2) Under low heat flux conditions resulting in small wall-bulk temperature differences—where thermophysical properties can be treated as constants—Bejan's correlations for entropy generation rate remain valid when using nanofluid-specific thermophysical properties. The SST k-ω-φ-α model accurately predicted both components of the entropy generation rate ($S'_{gen,f}$ and $S'_{gen,h}$), confirming its reliability for thermodynamic analysis.

(3) For cases with small wall-bulk temperature differences, increasing the nanoparticle volume fraction has opposing effects: it slightly reduces $S'_{gen,h}$ by enhancing thermal conductivity, while dramatically increases $S'_{gen,f}$ due to a significant increase in dynamic viscosity. Since $S'_{gen,f}$ is about three orders of magnitude greater than $S'_{gen,h}$, it dominates the total entropy generation. Thus, nanoparticle addition raises total irreversibility, potentially undermining thermodynamic performance in conventional channel flows under low heat flux.

(4) Under high heat flux conditions leading to large wall-bulk temperature differences, the classical Bejan's correlations for entropy generation rates are no longer valid. Accurate analysis must rely on the fundamental local definitions of entropy generation rates (Eqs. (26) and (27)), which require precise velocity and temperature fields. Moreover, using bulk temperature instead of wall temperature for property evaluation under large temperature differences significantly exacerbates errors in friction factor prediction.

(5) When the entropy generation rates due to friction ($S'_{gen,f}$) and heat transfer ($S'_{gen,h}$) become comparable, the total entropy generation rate (S'_{gen}) varies non-monotonically with Re for any given nanoparticle volume fraction (α_p), indicating the existence of an optimal Re that minimizes S'_{gen}. Moreover, the effect of increasing α_p on thermodynamic performance depends on the flow regime: it is beneficial at lower Re by reducing S'_{gen}, but becomes detrimental at higher Re by increasing it.

Future investigations will aim to address the aforementioned limitations by focusing on the following key aspects:

(1) The applicability of the model to other nanofluids with spherical nanoparticles (e.g., Cu, CuO, TiO_2);
(2) The performance of the SST k-ω-φ-α model in predicting flow and heat transfer in complex geometries;
(3) The capability of the SST k-ω-φ-α model for nanofluids containing non-spherical nanoparticles;
(4) The performance of the SST k-ω-φ-α model in predicting non-Newtonian flow behavior of nanofluids;
(5) Integrate the Brownian motion and thermophoresis terms into the governing equations to provide a more mechanistic insight into real nanofluid systems.

Acknowledgement: None.

Funding Statement: This research was funded by the Natural Science Foundation of Shenzhen, China (Grant No. 20220809155933002).

Author Contributions: The authors confirm contribution to the paper as follows: conceptualization, Xianglong Yang and Lei Yang; methodology, Yiyun Hu and Xianglong Yang; software, Yiyun Hu and Xianglong Yang; validation, Xianglong Yang and Lei Yang; writing—original draft preparation, Yiyun Hu and Xianglong Yang; writing—review and editing, Xianglong Yang and Lei Yang; project administration, Lei Yang; funding acquisition, Lei Yang. All authors reviewed and approved the final version of the manuscript.

Availability of Data and Materials: Data available on request from the authors.

Ethics Approval: Not applicable.

Conflicts of Interest: The authors declare no conflicts of interest.

Abbreviations

The following abbreviations are used in this manuscript

CFD	Computational Fluid Dynamics
EGA	Entropy Generation Analysis
SST	Shear Stress Transport
RANS	Reynolds-Averaged Navier-Stokes

Nomenclature

Lattin letters

a	Accelaration, m/s^2
a_1	Model constant
C_D	Interaction diffusion of turbulence
c_p	The specific heat, J/(kg·s)
d	Diameter of the nanoparticles, nm
D	Diameter of the circular tube, mm
f	Drag function; friction factor; specific term in turbulence model
F	Blending function
G	Production of turbulent kinetic energy
I	Turbulence intensity
k	Kinetic energy of turbulence, m^2/s^2
L	Length of the computational region, m
Nu	Nusselt number
p	Pressure, Pa
r	Radial coordinate, m
Re	Reynolds number
S'	Entropy generation rate per unit length, W/(m·K)
S'''	Entropy generation rate per unit volume, $W/(m^3 \cdot K)$
T	Temperature, K; turbulence time scale, s
t	Time, s
u,U	Velocity, m/s
$\vec{v}$	Velocity vector, m/s
x,y	Coordinates, m

Greek symbols

α	Elliptic variable in turbulence model; volume fraction
β	Model coefficient
γ	Model coefficient
ε	Dissipation rate, m^2/s^3
λ	Thermal conductivity, W/(m·K)
σ	Model coefficient
μ	Fluid dynamic viscosity, kg/(m·s)
ρ	Density, kg/m^3
τ	Particulate relaxation time, s; wall shear stress, Pa
φ	Wall-normal turbulent anisotropy

ω Specific dissipation rate of turbulence, 1/s

Subscripts

bf Base fluid
dr Drift velocity
f Friction
gen Entropy generation rate
h Heat transfer
i Interfacial; index i = 1, 2, 3
k Kinetic energy of turbulence
m Mixture
nf Nanofluid
t Turbulent
p Phase index, nanoparticle
q Phase index
w Wall

References

1. Choi SUS, Eastman JA. Enhancing thermal conductivity of fluids with nanoparticles. In: Proceedings of the ASME International Mechanical Engineering Congress and Exposition; 1995 Nov 12–17; San Francisco, CA, USA.
2. Pak BC, Cho YI. Hydrodynamic and heat transfer study of dispersed fluids with submicron metallic oxide particles. Exp Heat Transf. 1998;11(2):151–70. doi:10.1080/08916159808946559.
3. Xuan Y, Li Q. Investigation on convective heat transfer and flow features of nanofluids. J Heat Transf. 2003;125(1):151–5. doi:10.1115/1.1532008.
4. Heyhat MM, Kowsary F, Rashidi AM, Alem Varzane Esfehani S, Amrollahi A. Experimental investigation of turbulent flow and convective heat transfer characteristics of alumina water nanofluids in fully developed flow regime. Int Commun Heat Mass Transf. 2012;39(8):1272–8. doi:10.1016/j.icheatmasstransfer.2012.06.024.
5. Azmi WH, Hamid KA, Usri NA, Mamat R, Mohamad MS. Heat transfer and friction factor of water and ethylene glycol mixture based TiO_2 and Al_2O_3 nanofluids under turbulent flow. Int Commun Heat Mass Transf. 2016;76(4):24–32. doi:10.1016/j.icheatmasstransfer.2016.05.010.
6. Williams W, Buongiorno J, Hu LW. Experimental investigation of turbulent convective heat transfer and pressure loss of alumina/water and zirconia/water nanoparticle colloids (nanofluids) in horizontal tubes. J Heat Transf. 2008;130(4):042412. doi:10.1115/1.2818775.
7. Namburu PK, Das DK, Tanguturi KM, Vajjha RS. Numerical study of turbulent flow and heat transfer characteristics of nanofluids considering variable properties. Int J Therm Sci. 2009;48(2):290–302. doi:10.1016/j.ijthermalsci.2008.01.001.
8. Bianco V, Manca O, Nardini S. Numerical simulation of water/Al_2O_3 nanofluid turbulent convection. Adv Mech Eng. 2010;2:976254. doi:10.1155/2010/976254.
9. Ganesan P, Behroyan I, He S, Sivasankaran S, Sandaran SC. Turbulent forced convection of Cu-water nanofluid in a heated tube: improvement of the two-phase model. Numer Heat Transf Part A Appl. 2016;69(4):401–20. doi:10.1080/10407782.2015.1081019.
10. Kumar N, Puranik BP. Numerical study of convective heat transfer with nanofluids in turbulent flow using a Lagrangian-Eulerian approach. Appl Therm Eng. 2017;111(3):1674–81. doi:10.1016/j.applthermaleng.2016.08.038.
11. Cieśliński JT. Numerical modelling of forced convection of nanofluids in smooth, round tubes: a review. Energies. 2022;15(20):7586. doi:10.3390/en15207586.
12. Bejan A. Entropy generation minimization: the method of thermodynamic optimization of finite-size systems and finite-time processes. Boca Raton, FL, USA: CRC Press; 2013.
13. Jin Y. Second-law analysis: a powerful tool for analyzing computational fluid dynamics (CFD) results. Entropy. 2017;19(12):679. doi:10.3390/e19120679.

14. Singh PK, Anoop KB, Sundararajan T, Das SK. Entropy generation due to flow and heat transfer in nanofluids. Int J Heat Mass Transf. 2010;53(21–22):4757–67. doi:10.1016/j.ijheatmasstransfer.2010.06.016.
15. Moghaddami M, Mohammadzade A, Esfehani SAV. Second law analysis of nanofluid flow. Energy Convers Manag. 2011;52(2):1397–405. doi:10.1016/j.enconman.2010.10.002.
16. Sohel MR, Saidur R, Hassan NH, Elias MM, Khaleduzzaman SS, Mahbubul IM. Analysis of entropy generation using nanofluid flow through the circular microchannel and minichannel heat sink. Int Commun Heat Mass Transf. 2013;46(9):85–91. doi:10.1016/j.icheatmasstransfer.2013.05.011.
17. Bianco V, Manca O, Nardini S. Entropy generation analysis of turbulent convection flow of Al_2O_3–water nanofluid in a circular tube subjected to constant wall heat flux. Energy Convers Manag. 2014;77(17–18):306–14. doi:10.1016/j.enconman.2013.09.049.
18. Mohseni-Gharyehsafa B, Ebrahimi-Moghadam A, Okati V, Farzaneh-Gord M, Ahmadi MH, Lorenzini G. Optimizing flow properties of the different nanofluids inside a circular tube by using entropy generation minimization approach. J Therm Anal Calorim. 2019;135(1):801–11. doi:10.1007/s10973-018-7276-x.
19. Mukherjee S, Aljuwayhel NF, Bal S, Mishra PC, Ali N. Modelling, analysis and entropy generation minimization of Al_2O_3-ethylene glycol nanofluid convective flow inside a tube. Energies. 2022;15(9):3073. doi:10.3390/en15093073.
20. Yang X, Yang L. Numerical study of entropy generation in fully developed turbulent circular tube flow using an elliptic blending turbulence model. Entropy. 2022;24(2):295. doi:10.3390/e24020295.
21. Mwesigye A, Huan Z. Thermodynamic analysis and optimization of fully developed turbulent forced convection in a circular tube with water-Al_2O_3 nanofluid. Int J Heat Mass Transf. 2015;89:694–706. doi:10.1016/j.ijheatmasstransfer.2015.05.099.
22. Ji Y, Zhang HC, Yang X, Shi L. Entropy generation analysis and performance evaluation of turbulent forced convective heat transfer to nanofluids. Entropy. 2017;19(3):108. doi:10.3390/e19030108.
23. Rashidi MM, Nasiri M, Shadloo MS, Yang Z. Entropy generation in a circular tube heat exchanger using nanofluids: effects of different modeling approaches. Heat Transf Eng. 2017;38(9):853–66. doi:10.1080/01457632.2016.1211916.
24. Behzadmehr A, Saffar-Avval M, Galanis N. Prediction of turbulent forced convection of a nanofluid in a tube with uniform heat flux using a two phase approach. Int J Heat Fluid Flow. 2007;28(2):211–9. doi:10.1016/j.ijheatfluidflow.2006.04.006.
25. Behroyan I, Ganesan P, He S, Sivasankaran S. Turbulent forced convection of Cu-water nanofluid: CFD model comparison. Int Commun Heat Mass Transf. 2015;67(4):163–72. doi:10.1016/j.icheatmasstransfer.2015.07.014.
26. Bazdidi-Tehrani F, Vasefi SI, Anvari AM. Analysis of particle dispersion and entropy generation in turbulent mixed convection of CuO-water nanofluid. Heat Transf Eng. 2019;40(1–2):81–94. doi:10.1080/01457632.2017.1404828.
27. Durbin PA. Near-wall turbulence closure modeling without "damping functions". Theor Comput Fluid Dyn. 1991;3(1):1–13. doi:10.1007/BF00271513.
28. Manceau R, Hanjalić K. Elliptic blending model: a new near-wall Reynolds-stress turbulence closure. Phys Fluids. 2002;14(2):744–54. doi:10.1063/1.1432693.
29. Billard F, Revell A, Craft T. Application of recently developed elliptic blending based models to separated flows. Int J Heat Fluid Flow. 2012;35(2):141–51. doi:10.1016/j.ijheatfluidflow.2012.04.012.
30. Manceau R. Recent progress in the development of the elliptic blending Reynolds-stress model. Int J Heat Fluid Flow. 2015;51(9):195–220. doi:10.1016/j.ijheatfluidflow.2014.09.002.
31. Durbin PA. Some recent developments in turbulence closure modeling. Annu Rev Fluid Mech. 2018;50(1):77–103. doi:10.1146/annurev-fluid-122316-045020.
32. Yang XL, Liu Y, Yang L. A shear stress transport incorporated elliptic blending turbulence model applied to near-wall, separated and impinging jet flows and heat transfer. Comput Math Appl. 2020;79(12):3257–71. doi:10.1016/j.camwa.2020.01.024.
33. Yang X, Yang L. Numerical simulation of high-pressure water jets in air by an elliptic-blending turbulence model: a parametric study. Mathematics. 2025;13(10):1646. doi:10.3390/math13101646.
34. ANSYS, Inc. ANSYS fluent theory guide. Canonsburg, PA, USA: ANSYS, Inc.; 2024.
35. Mohammadi M. Numerical study of turbulent nanofluid flow in double-tube heat exchanger: the role of second law analysis. Arab J Sci Eng. 2023;48(9):12269–90. doi:10.1007/s13369-023-07732-w.

36. Laue LK, Hattel J, Mostafazade Abolmaali A. CFD investigation of thermo-hydraulic performance enhancement in a double-pipe heat exchanger using non-uniformly spaced perforated ring inserts. Energy Convers Manag. 2026;355(5):121293. doi:10.1016/j.enconman.2026.121293.
37. Masuda H, Ebata A, Teramae K, Hishinuma N. Alteration of thermal conductivity and viscosity of liquid by dispersing ultra-fine particles. dispersion of Al_2O_3, SiO_2 and TiO_2 ultra-fine particles. Netsu Bussei. 1993;7(4):227–33. doi:10.2963/jjtp.7.227.
38. Menter F, Ferreira JC, Esch T, Konno B. The SST turbulence model with improved wall treatment for heat transfer predictions in gas turbines. In: Proceedings of the International Gas Turbine Congress; 2003 Nov 2–7; Tokyo, Japan. p. 2–7.
39. Ghajar AJ, Cengel YA. Heat and mass transfer: fundamentals and applications. 6th ed. New York, NY, USA: McGraw-Hill Education; 2020.
40. Ali A, Sajid M, Anjum HJ, Awais M, Nisar KS, Saleel CA. Entropy generation analysis of peristaltic flow of nanomaterial in a rotating medium through generalized complaint walls of micro-channel with radiation and heat flux effects. Micromachines. 2022;13(3):375. doi:10.3390/mi13030375.
41. Ali A, Ahmed M, Ahmad A, Nawaz R. Enhanced heat transfer analysis of hybrid nanofluid over a Riga plate: incorporating Lorentz forces and entropy generation. Tribol Int. 2023;188(5):108844. doi:10.1016/j.triboint.2023.108844.
42. Lakhdar A, Skander J, Tayeb NT, Mostefa T, Hossain S, Kim SM. Analysis of entropy generation for mass and thermal mixing behaviors in non-Newtonian nano-fluids of a crossing micromixer. Micromachines. 2024;15(11):1392. doi:10.3390/mi15111392.